

Optical spectroscopy of the dwarf nova U Geminorum

E. Unda-Sanzana, T. R. Marsh, L. Morales-Rueda

¹ *Instituto de Astronomía, Universidad Católica del Norte, Antofagasta, Chile; eundas@almagesto.org*

² *Dept. of Physics, University of Warwick, Coventry, United Kingdom CV4 7AL; t.r.marsh@warwick.ac.uk*

³ *Dept. of Astrophysics, University of Nijmegen, 6500 GL Nijmegen, The Netherlands; lmr@astro.ru.nl*

Accepted . Received ; in original form

ABSTRACT

The dwarf nova U Gem is unique in having a direct measurement of the K -velocity of its white dwarf from *HST* spectra ($K_1 = 107 \pm 2 \text{ km s}^{-1}$, Long et al. 1999). We present high-resolution optical spectra of the dwarf nova U Gem in quiescence taken to test the accuracy to which the *HST* value can be recovered from optical data. We find that, even with data of very high signal-to-noise ratio on this archetypal system, we cannot recover Long et al.’s value to better than about 20% by any method. Contamination by neighbouring emission lines seems a likely culprit. Our data reveal a number of new features: Doppler tomograms show emission at low velocity, close to the centre of mass, and a transient, narrow absorption feature is seen in the Balmer lines near the line centres at the time of eclipse. We suggest that stellar prominences, as previously invoked for the dwarf novae IP Peg and SS Cyg in outburst, may explain both of these features. The He II 4686.75 Å line emission is dominated by the gas stream/disc impact region. Two distinct spots are seen in Doppler maps, the first being very narrow and showing a velocity close to that of the accretion disc in the impact region, and the second much broader and located between the velocities of the (ballistic) stream and the (Keplerian) disc. We present tentative evidence of weak spiral structure, which may support explanations for “spiral shocks” based upon 3-body effects. We find no evidence of stream-disc overflow in the system. Our data suggests an inclination angle $> 70^\circ$, adding to the evidence supporting the existence of a puzzle in the mass of U Gem’s white dwarf. The mass donor is clearly seen in the Doppler maps, with emission concentrated towards its poles, and mainly on the side facing the white dwarf. This suggests irradiation with shielding by the disc from which we estimate an H/R ratio between 0.15 and 0.25.

Key words: binaries: close – binaries: eclipsing – binaries: spectroscopic – stars: individual: U Gem

1 INTRODUCTION

Theoretical models of the evolution of cataclysmic variables (CVs) make predictions about the distributions of their physical parameters such as orbital period, mass ratio and the individual masses of the two stars. If these parameters can be measured, the (many) assumptions that go into the theory can be tested. These assumptions are of interest in the broader context of binary star evolution. The same parameters are needed to gain an accurate understanding of the accretion processes which dominate these stars. Unfortunately, the only reliable physical parameter that can be measured for the majority of CVs is their orbital period, with perhaps the spectral type of the donor star coming a distant second. In this ranking, the masses of the white dwarf and the donor star are so uncertain that they are often barely mentioned in the context of evolution. This is

partly because of the difficulty of measuring orbital inclinations common to all forms of close binary, but also because it is hard to measure the radial velocities of the binary components.

The optical spectra of most CVs are dominated by emission from accreting material, rather than the white dwarf. In the case of non-magnetic systems, the emission lines are formed in discs, and often have a double-peaked shape resulting from the Doppler shift of matter rotating in a Keplerian disc. The high-velocity wings of the emission lines are expected to form close to the white dwarf, where it is hoped the flow is axi-symmetric. If so, these wings should trace the motion of the white dwarf. This is the idea behind many studies of CVs. However, this method fails in practice: in those systems in which one has independent knowledge of the orbital phase, the emission line radial velocities

arXiv:astro-ph/0604396v1 18 Apr 2006

invariably fail to match expectations (Stover 1981). Nevertheless, the white dwarf velocities measured in this way are still used for mass determination, perhaps because there has not been any direct evidence for the magnitude of the distortion. This changed after Long & Gilliland (1999) measured directly the radial velocity semi-amplitude of the white dwarf in U Gem from narrow photospheric lines visible in the ultraviolet. In this case, the phase agreed perfectly with the predicted conjunction phase. Long & Gilliland (1999) measured $K_1 = 107 \pm 2 \text{ km s}^{-1}$. The direct nature of this measurement makes it the most accurate to date for any CV, and gives us the chance to test what the nature of the distortion of the emission line measurements in one system at least. One other CV for which we have a good estimate of K_1 is AE Aqr (Welsh et al 1995). In this case K_1 is measured from the pulsations of the white dwarf. However, AE Aqr is a very unusual CV with flaring emission lines that are not suited to testing the general method of measuring K_1 from line emission.

U Gem is interesting from several other points of view: it is a double-lined, partially-eclipsing system, and is one of the brightest dwarf novae. It has prominent emission from the gas stream/disc impact region which has a velocity in-between that of a Keplerian disc and a ballistic stream (Marsh et al. 1990). Finally, during outburst it has shown spiral shocks (Groot 2001). We will see that our new data has something to tell us on all of these issues.

2 OBSERVATIONS AND REDUCTION

The observations were taken in January 2001 at La Palma (see Table 1 for details). The 4.2-m William Herschel Telescope (WHT) was used with the double-beamed ISIS spectrograph. Two datasets, covering wavelength ranges around $H\alpha$ and $H\beta$ were acquired using the highest resolution gratings. The spectrograph’s slit was oriented at a position angle of 150.6° to include a comparison star for slit loss corrections.

The spectrophotometric standard HD19445 and one featureless star were observed during the nights with best seeing ($\sim 0.7''$) for flux calibration and to remove the effect of telluric lines on the red data (Bessell 1999). Flat-fields and comparison arc spectra were taken approximately every 60 minutes for the red and the blue dataset. The weather was clear throughout most of our run with seeing of order 1 arcsecond for most of it.

The spectra were optimally extracted (Marsh 1989), with flat fields interpolated from the many taken during the night. The wavelength scales were interpolated from the nearest two arc spectra. Slit losses were corrected using the ratio of the spectra of the comparison star to a spectrum taken with a wide slit close to the zenith.

3 RESULTS

3.1 Average spectrum

Fig. 1 shows the average spectrum of U Gem during our run. U Gem shows broad Balmer ($H\alpha$, $H\beta$) and Fe II 4923.92 Å (hereafter Fe II) emission. He I 6678.149 Å (hereafter He I) and the high excitation line He II 4685.750 Å (hereafter He II)

are also present, the latter only obvious in trailed spectra however. Next to Fe II 4923.92 there is emission at an unidentified wavelength (Fe II 5018.44 Å or He I 5015), which, as we will see later, introduces some contamination in Fe II.

The B -band line profiles show the double-peaked structure often seen in CVs, and attributed to the presence of a rotating accretion disc around the compact object. The R -band profiles exhibit a central stationary component which is reminiscent of similar features seen in a handful of other systems. We discuss this component in detail in Section 3.4.2.

3.2 Light curves

We computed light curves of sections of the continuum, avoiding emission lines (6400-6480 Å, 4620-4650 Å and 4720-4470 Å), and also of emission lines after continuum subtraction, summing the flux within 2000 km s^{-1} of the line centre. Exceptions were made for Fe II, for which we used the range from -1500 to $+1500 \text{ km s}^{-1}$ in order to prevent contamination from the wings of $H\beta$, and He II for which we used $\pm 650 \text{ km s}^{-1}$ due to the narrowness of the emission. The results are plotted in Figure 2. We used the ephemeris of Marsh et al. (1990) updated from a recent measurement of the inferior conjunction of the red star (Naylor et al. 2005) so that zero phase occurs at $\text{TDB} = 2451915.8618 \pm 0.0002$.

Both the blue and the red continuum light curves display smooth, moderately deep, narrow eclipses just after phase 0. This is the eclipse of the gas stream/disc impact region, or “bright-spot” at the edge of the disc. The white dwarf is not eclipsed in U Gem

The light curves of $H\alpha$ and $H\beta$ show broad humps around phases 0.25 and 0.75. The humps are more marked in $H\alpha$, which makes us think that they are largely due to ellipsoidal modulations produced by the Roche deformation of the mass donor, which we expect to be stronger in red light. The more complex structure of the hump in 0.75 is expected if that one is caused by a mixture of ellipsoidal modulations and variations in the strength of emission from the bright-spot. The light curves also display a shallow eclipse roughly centred around phase 0, and extending symmetrically ~ 0.1 in phase to both sides. This is produced by the mass donor passing in front of the outer part of the accretion disc.

In He II the eclipse occurs slightly after phase 0. We will see in the following sections that this is because He II is dominated by emission from the bright-spot. The peak of light near phase 0.9 is consistent with the orbital humps detected in the continua. By contrast, the Balmer lines are hardly eclipsed indicative of a relatively small contribution from the bright-spot to these lines.

The light curve of He I is strongly modulated, with the peak flux at phase 0.3-0.4 caused by an increase in the contribution of the bright-spot (discussed in the following sections).

3.3 Trailed spectra

Figures 3 and 4 show the average trailed spectra. Emission lines of He II, $H\beta$ and Fe II, $H\alpha$ and He I are visible. The trailed spectra show a remarkably rich mix of features. Some of these are well-known from earlier work on U Gem (Stover

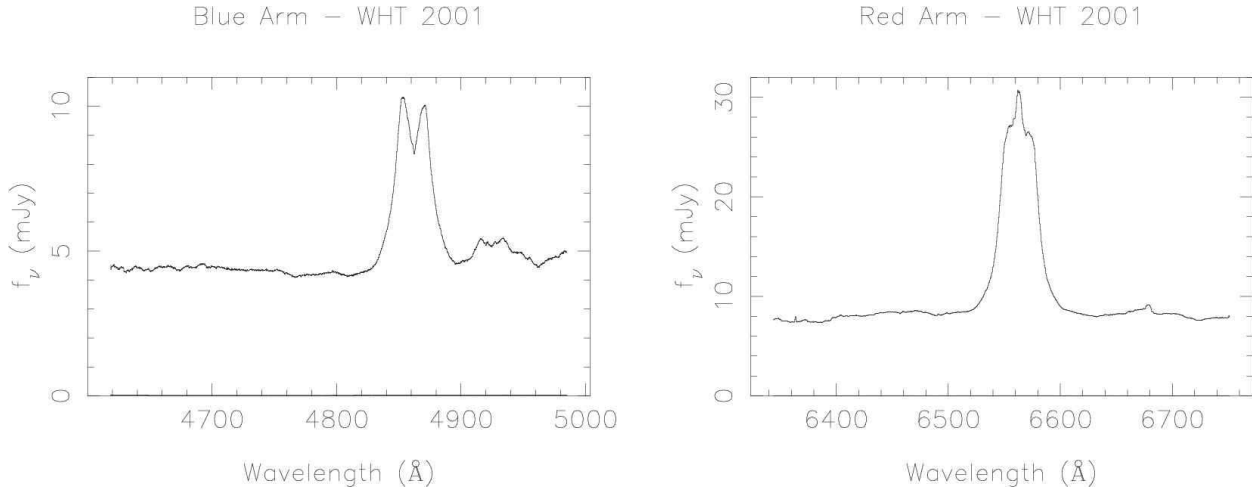


Figure 1. The average spectrum of U Gem. Note the change in the vertical scale between the two wavelength ranges.

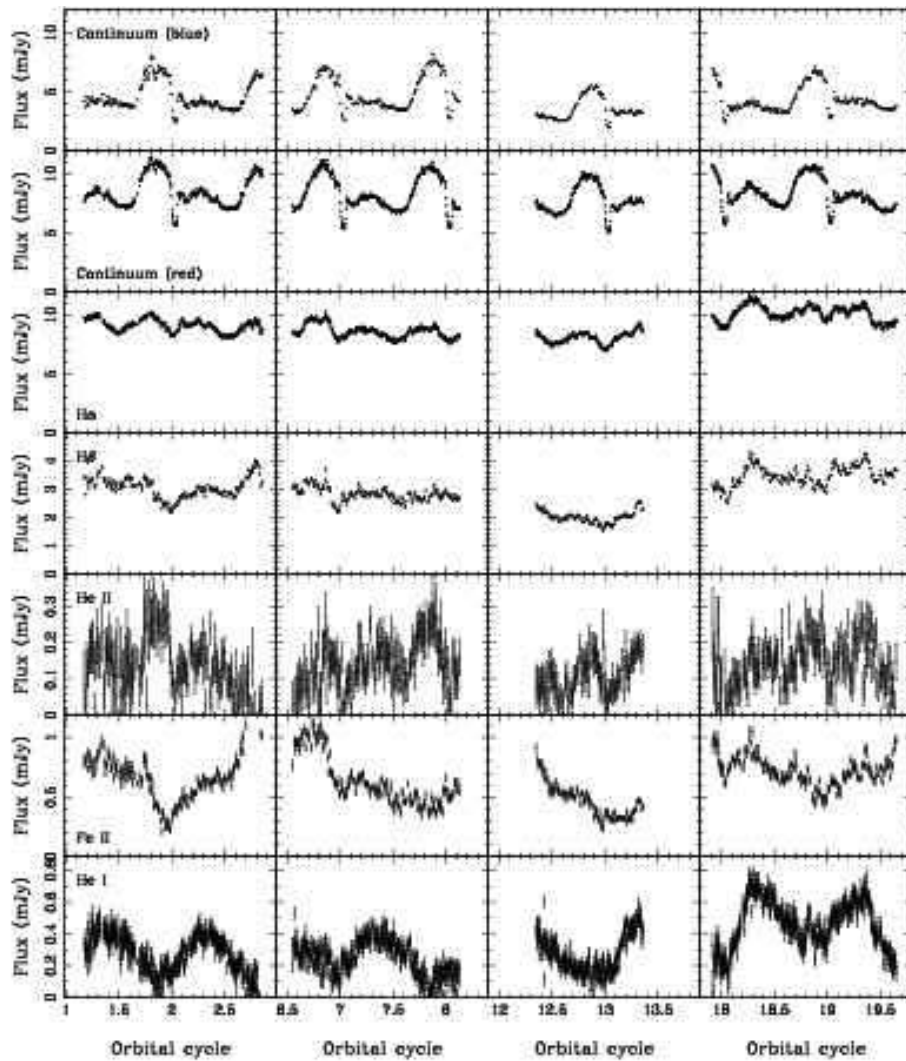
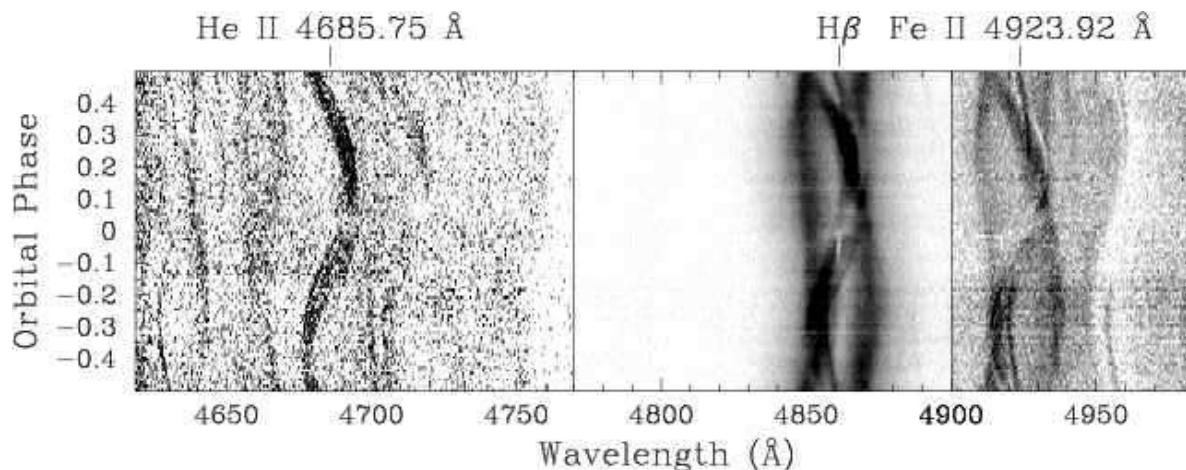


Figure 2. Continuum and emission light curves of the WHT/ISIS data. The zero-point of the phase is cycle 80740 on our ephemeris.

Table 1. Summary of the observations. In this table MD stands for 'mean dispersion'. T is the mean exposure time per frame and DT is the average dead time between exposures. N is the number of spectra obtained per night per arm.

CCD	Grating	Date	Start - End (UT)	Orbits covered	λ range (\AA)	MD (\AA pixel^{-1})	FWHM (\AA)	T/DT (s)	N
EEV12	H2400B	12/13 Jan 2001	22:14-05:32	1.719	4618-4985	0.21	0.42	120/12	182
TEK4	R1200R	12/13 Jan 2001	22:14-05:32	1.719	6343-6751	0.40	0.80	50/6	419
EEV12	H2400B	13/14 Jan 2001	21:08-03:54	1.594	4618-4985	0.21	0.42	120/12	176
TEK4	R1200R	13/14 Jan 2001	21:08-03:54	1.594	6343-6751	0.40	0.80	50/6	410
EEV12	H2400B	14/15 Jan 2001	21:44-02:07	1.032	4618-4985	0.21	0.42	120/12	112
TEK4	R1200R	14/15 Jan 2001	21:44-02:07	1.032	6343-6751	0.40	0.80	50/6	259
EEV12	H2400B	15/16 Jan 2001	21:22-04:49	1.755	4618-4985	0.21	0.42	120/12	191
TEK4	R1200R	15/16 Jan 2001	21:22-04:49	1.755	6343-6751	0.40	0.80	50/6	442

**Figure 3.** The blue spectra binned into 100 bins of orbital phase. To cope with the large dynamic range of the features we use 3 different normalisations running from the continuum level to 0.5, 7.0 and 2.0 mJy above continuum for Fe II, He II and Fe II respectively.

1981; Marsh et al 1990) and related systems; others are seen here for the first time.

The light curves discussed in Section 3.2 reveal some flaring, more conspicuous in $H\beta$. We looked for matches of this behaviour in the trailed spectra, finding good correspondence in the case of Balmer lines. The features are also stronger at high velocities. This indicates that the inner accretion disc is the likely source. We found no clear indication of these flares in He II, He I or Fe II.

3.3.1 Standard features in the trailed spectra

The lines show several well-known features of CV spectra such as double-peaked emission from the disc, an emission 'S'-wave from the gas stream/disc impact point and emission from the mass donor star. These occur with varying strength. The double-peaked emission from the discs is best seen in $H\beta$, while the emission from the donor star is most obvious in $H\alpha$ and Fe II (Fig. 3). The latter line in particular shows that the emission from the donor star fades around the time of eclipse, indicating that it is concentrated on the side facing the white dwarf. This suggests that the emission is triggered by irradiation from the accretion regions.

The bright-spot S-wave is especially clear in the light of He II (Fig. 3) which has no visible disc contribution at all. The He II trail reveals that the S-wave itself is split into two, with one broad component, but in addition a very nar-

row component which executes a somewhat different path from its companion. We discuss these in Section 3.4.1 after we present Doppler maps of our data. From the Doppler analysis we conclude that both these S-waves come from the bright-spot region.

The effect of the partial eclipse on the lines is relatively subtle in most lines, but is clearly seen in $H\alpha$ as a region of low flux running diagonally between the double-peaks from the lower-left towards the upper-right between phases 0.95 and 0.05. This is the effect of eclipsing Doppler-shifted emission from a prograde rotating disc (Greenstein & Kraft 1959; Young & Schneider 1980). We will use the eclipse in section 3.5 to measure the orbital inclination of U Gem.

We now look at new features revealed by the high signal-to-noise of our data.

3.3.2 Low-velocity absorption and emission

In $H\alpha$, but more obviously still in especially $H\beta$ (Figure 5), a narrow absorption feature appears at line centre immediately before eclipse between phases 0.91 and 0.98. To our knowledge, nothing like this feature has been seen before in U Gem or any other system. It could be present now either because of the improved data quality or because of a true change of structure in the system.

Also in $H\alpha$, and more clearly in He I, there is emission at low, almost zero velocity, visible as a vertical line in He I.

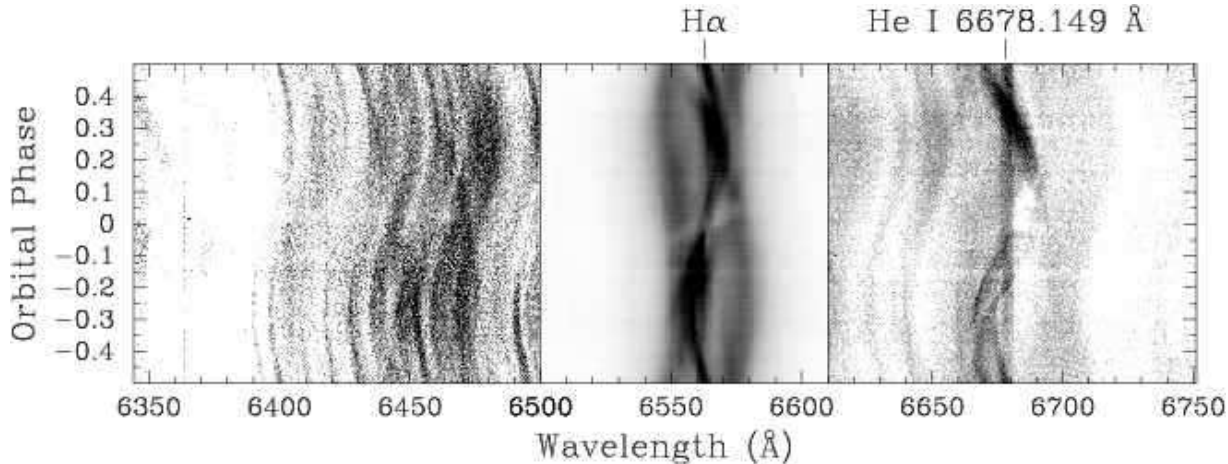


Figure 4. The red spectra binned into 200 bins of orbital phase. We reserve a panel to show the many features seen in the continuum near $H\alpha$. The maximum plotted levels are: 1, 28 and 2 mJy above the continuum level for the continuum region, $H\alpha$ and He I respectively.

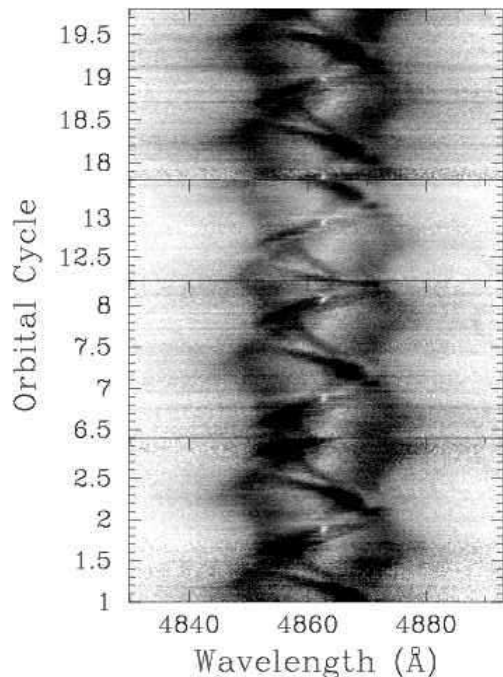


Figure 5. The $H\beta$ data without phase-binning. Cycle 0 has been set to the cycle 80740 according to the ephemeris used in this paper.

We refer to this as “the low-velocity emission”. Such emission is hard to understand because there is no part of the system that is stationary in this manner.

3.3.3 Low-level structure in the continuum

The continuum seen in Figure 4 shows a mass of lines at a low level of flux. In several of these lines a modulation is seen resembling the one produced by the mass donor’s orbital motion, so we attempted to track the source of the lines. To improve the S/N of this region we phase binned the spectra in 50 phases. Then we selected one of the spectra as a template and did a cross-correlation with the set of phase

binned data, backprojecting later the result in what is called a skew-map (Smith, Dhillon & Marsh 1998). This procedure showed that the features do indeed track the motion of the irradiated face of the donor, having the correct phase and a semi-amplitude $K = 210 \text{ km s}^{-1}$ (see Section 3.4.5).

We deduce that the features are line emission from the irradiated face of the donor. We could not make secure identifications for the lines, although several match the wavelengths of FeII lines.

3.4 Doppler tomography

To understand the features present in our trailed spectra, we used Doppler tomography to study the emission lines. This technique combines all the information observed in the trailed spectra and generates a representation of the system in velocity coordinates. Due to the current lack of understanding of how the system’s velocity coordinates should be translated to position coordinates, it is not possible to get a direct picture of the binary star, and so the interpretation is carried out in velocity coordinates. This allows a visual separation of the contributions from different parts of the binary star (e.g. the mass donor, the bright spot, the accretion disc, etc.), and permits comparison with theoretical predictions under some rough assumptions (e.g. Keplerian regime). For a thorough presentation of the subject see Marsh & Horne (1988).

In Figs. 6 and 7 we present the tomograms for the data. The spectra taken during eclipse were excluded from the computation of the maps, but they were included as a template for the calculation of the synthetic spectra computed back from the tomograms (third row from the top in the figures). We plot the outline of the Roche lobe of the mass donor over the tomograms. This was calculated by assuming $K_1 = 107.1 \text{ km s}^{-1}$ (Long & Gilliland 1999) and $K_2 = 298 \text{ km s}^{-1}$. We have already explained why K_1 is a good assumption. K_2 is a combination of the three published values (Wade 1981, Friend et al. 1990, Naylor et al. 2005), which are consistent with each other.

We plot two velocity trajectories. The lower of the two is the velocity of a ballistic gas stream. The upper one is the

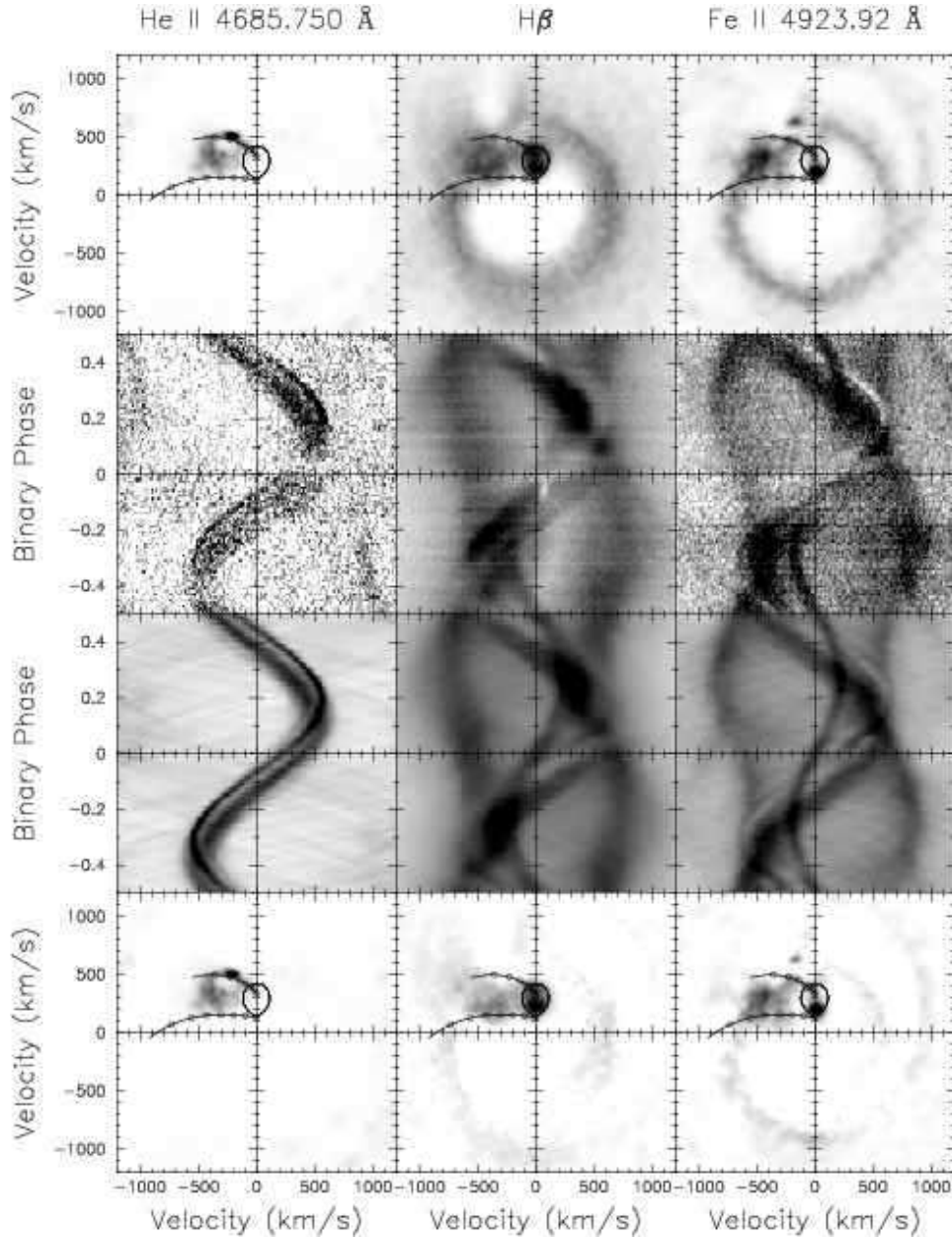


Figure 6. Doppler tomography for the blue arm. From top to bottom the rows show: 1) the Doppler tomograms, 2) the observed spectra from which the tomograms were calculated, 3) synthetic data computed from the tomograms, and 4) the tomograms after the symmetrical part around $(0, -107.1) \text{ km s}^{-1}$ was subtracted. The tomograms include an outline of the Roche lobe of the mass donor and two velocity trajectories for the stream. All scales start from zero with uppermost levels chosen to improve the visualization of details. With the exception of the third row (from top to bottom), which is evenly saturated at 90 per cent of the peak flux, the first column is saturated at 50 per cent, the second at 80 per cent, and the third at 60 per cent. See text for a thorough description of the features seen in the tomograms.

velocity of the disc, assuming a Keplerian field, at positions along the stream. The distance to the white dwarf is marked in these paths by small circles at intervals of 0.1 times the distance of the inner Lagrangian point (R_{L1}). Each trajectory is plotted from $1.0R_{L1}$ to $0.4R_{L1}$ (leftmost value).

As expected from the discussion of the trailed spectra, neither the disc nor the mass donor is detected in the He II tomogram but the bright spot is clearly resolved. In He I the disc is almost undetectable, but both the mass donor and the bright spot have strong emission. Additionally, the He I and

H α tomograms show a blob of emission around the centre of mass of the system, the tomographic equivalent of the “low velocity emission” we discussed earlier. Both the disc and the mass donor are clearly seen in H α , H β and Fe II, the bright spot appearing with varying degrees of strength. The presence of the mass donor in these tomograms is used later for a study of disc shielding (Section 3.4.5).

The tomogram for Fe II displays two extra features. First, rather like He II, there is a very sharp spot seen above the path of Keplerian disc velocities. Immediately below this

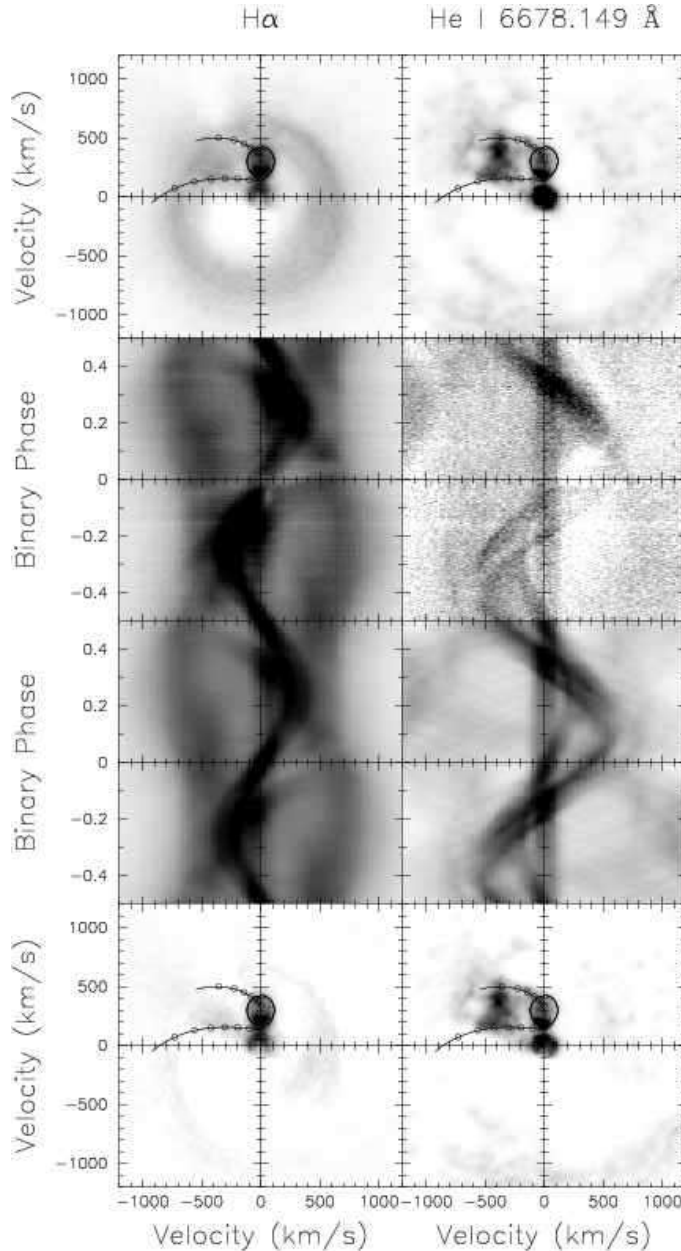


Figure 7. Doppler tomography for the red arm. See Fig. 6 for further details of the display. With the exception of the third row (from top to bottom), which is evenly saturated at 90 per cent of the peak flux, the left column is saturated at 80 per cent and the right column at 70 per cent.

spot there is a low intensity region. This corresponds to the absorption line 'S'-wave seen in the trailed spectrum of this line (Fig. 6). This is probably the absorption equivalent of the sharp emission seen in He II. However, because this is only seen clearly over a very restricted range of phases (0.15 to 0.45), the emission spot gives a phase modulation – in other words it is likely to be an artefact and its displacement from the He II emission spot is probably not significant. We conclude that both the He II emission and Fe II absorption come from the same well-defined structure associated with the gas stream impact. The spiral seen in the upper-right quadrant of the Fe II map is caused by the contamination

from a nearby line which can be seen on the right-hand side of the trailed spectrum.

The bottom row in Figures 6 and 7 show the tomograms after we subtracted the symmetrical part around $(0, -107.1) \text{ km s}^{-1}$. Even after discarding the contamination in Fe II, we still see spiral structure in this map, and also in H α and H β . This is further discussed in Section 3.4.4.

3.4.1 Location of the bright spot

In addition to the sharp bright spot close to the Keplerian stream trajectory that we see in the He II map, we find a diffuse blob of emission. This is located along the line that

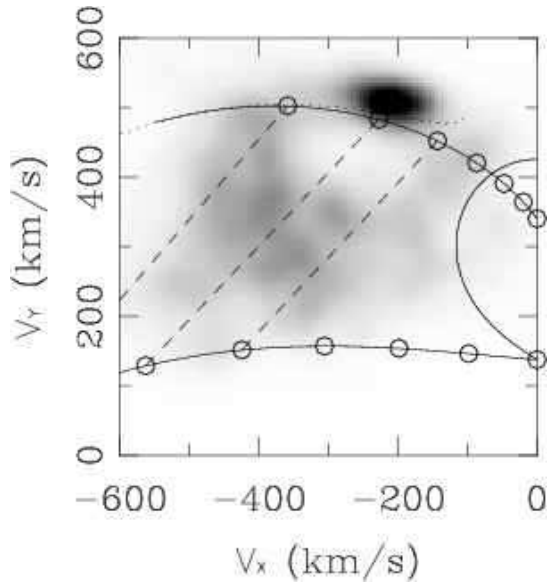


Figure 8. Blow up of the He II tomogram in the bright spot region. The dashed lines connect the velocity of the ballistic gas stream (black lower trajectory) and the velocity on the Keplerian disc along the gas stream (black upper trajectory) for the same points at distances of 0.4 , 0.5 and $0.6 R_{L1}$ to the white dwarf (right to left). For the dotted trajectory see text.

connects the sharp feature to the matching spatial point that has the ballistic velocity predicted for the stream (see Figure 8), at $\sim 0.5 R_{L1}$. The presence of the blob indicates that a mixture of velocities coexist in the bright spot, the stream adjusting to the velocities on the outer zones of the Keplerian disc (already noted by Marsh et al. 1990). The value $\sim 0.5 R_{L1}$ (0.3 in units of the orbital separation a) is consistent with observations by Smak (1984) and is smaller than the radius of the tidally limited accretion disc ($0.44a$, see Warner 1995).

Assuming that the position of the bright spot did not change significantly during our observations, we can use the sharp feature to estimate the bright spot’s azimuthal location by treating the gas stream/disc impact point as a point corotating like a rigid body with the system. We conclude that the bright spot is face-on when the system reaches phase ~ 0.95 , which is compatible with previous results obtained from reconstructed light curves (e.g. Smak 1971).

The agreement between the position of the sharp feature and the predicted path is not perfect, so we turn our attention to possible causes. The path for the Keplerian disc velocities changes with K_2 , so one possibility is that a better value of K_2 is needed, the problem being that measurements of K_2 are affected by irradiation and the corrections needed are not entirely certain (Friend et al 1990; Naylor et al 2005). We calculate that $K_2 \sim 315 \text{ km s}^{-1}$ produces a good fit. This value for K_2 is not much higher than the published values, i.e. $283 \pm 15 \text{ km s}^{-1}$ (Wade 1981), $298 \pm 9 \text{ km s}^{-1}$ (Friend et al. 1990), 302 km s^{-1} (Naylor et al 2005). Still, it is worth considering other possible causes.

The predicted stream path is based upon circular, Keplerian orbits within the disc. However, the disc should be distorted by 3-body effects, especially in its outer regions (Paczynski 1977). We computed the velocity of the Keple-

rian disc along the path of the stream allowing for such effects. The results are plotted as the dotted line in Fig. 8, extending as far as the largest non-intersecting orbit at $\sim 0.6 R_{L1}$. At radii smaller than $\sim 0.4 R_{L1}$ the three body effects are negligible, but they do alter the predicted velocities in the right direction, although not by enough on their own. Now however, K_2 need only be $\sim 308 \text{ km s}^{-1}$ to fit, which is compatible with Wade’s, Friend et al’s and Naylor et al’s measurements.

Perhaps the most remarkable characteristic of the spot is how narrow it is, being unresolved even at a resolution of $R \approx 10,000$. This, and the close match to the Keplerian disc velocity along the stream, suggests that it must come from the disc immediately prior to the stream/disc impact region. It could only do so by irradiation from the main impact site. This does not give a corresponding feature at the ballistic stream velocity, possibly because of the lower density of the stream.

In contrast with the narrow spot in He II, the other maps show a more diffuse feature which lies between the two predicted stream paths. Marsh et al (1990) ascribed this emission to the post-impact flow, with gas taking a velocity intermediate between the ballistic stream and the Keplerian disc. The extraordinary feature of this emission, which was not clear at the lower resolution of Marsh et al’s study, is that it appears to extend all the way to the secondary star (Figs 6 and Fig. 7). This should not be possible because it would require the disc to extend well beyond its tidal radius. There is a similar extension to high velocities which we will discuss in following sections. We have no explanation for either of these features.

3.4.2 Low velocity emission

In the case of the H α Doppler map, the low velocity emission is oddly asymmetric, displaying an elongated crescent-moon (Fig. 7). After subtracting the symmetrical part around $(0, -107.1) \text{ km s}^{-1}$ from the tomogram, the blob reveals again a crescent shape. North et al. (2001) found a similar shape in V426 Oph’s low velocity emission.

Similar low velocity emission has been reported for other CVs. A summary of such reports is given in Table 2. There is no reason for any component of the system to be at rest near the centre of mass, unless the mass ratio q has an extreme value. This is the case for example for GP Com for which $q \sim 0.02$ allows one to make the case for the white dwarf to be responsible for the low-velocity emission it displays (Morales-Rueda et al. 2003). In all the other cases the emission is seen either at the centre of mass or somewhat displaced towards the mass donor. Steeghs et al. (1996) suggested that the emission was from gas originating in the mass donor, but trapped in a prominence produced by a combination of magnetic, gravitational and centrifugal forces within the rotating binary system. The prominence would then be irradiated by the compact object and the disc, allowing its detection as a component corotating as a rigid body with the mass donor.

These “slingshot prominences”, if similar to the prominences observed in single stars, could be located up to several radii from the magnetic star (e.g. Collier Cameron et al. 1990). If the prominence behaves like the ones we observe on the Sun and rapidly rotating stars like AB Dor (see

Collier Cameron et al. 1999), we should expect them to be short-lived. Four nights should perhaps have hinted at a variation either in flux or in size, but the feature is consistent from night to night. On the other hand, there is evidence that loops on single stars could last ~ 1 d (γ Cas, Smith et al. 1998). Perhaps under certain conditions prominences could last for longer. There might be a common origin for the low velocity emission and the low velocity absorption (section 3.3.2) if the gas trapped in the prominences passes across the white dwarf at the time of eclipse, which seems quite possible.

3.4.3 Stream-disc overflow?

Simulations of the stream in U Gem by Kunze et al. (2001) predict that more than half the stream overflows the outer edge of the disc. With high signal-to-noise ratio and smooth disc profiles, our data are very well suited to detection of such overflow which can be expected to cause emission along the path of the stream up to the point of closest approach to the white dwarf (Livio et al. 1986; Armitage & Livio 1998; Lubow 1989). In U Gem the point of closest approach is $\sim 0.13 R_{L1}$ from the white dwarf, and in velocity space corresponds to a region in the lower right quadrant of the Doppler maps of Figs 6 and 7. To search more rigorously, we subtract the smooth background from the disc by using an elliptical isophote fitting procedure described in Appendix A. After performing the subtraction we obtained the tomograms seen in Fig. 9, which are scaled to only 3% of the peak height of the raw tomograms. The bright spot is clear in the maps, but there is no evidence of stream-disc overflow along the path of the stream even at this low level. In order to quantify this result we measured averages and peak values over several samples of the region along which the hypothetical overflow would travel, before and after the subtraction of the elliptical continuum. By comparing those values we conclude that any possible overflow would contribute less than $3 \pm 2\%$ to the flux from the disc surface.

Fig. 9 does show an excess extending up and to the left of the main disc/stream impact region to well over 1000 km s^{-1} . A similar effect was seen in EX Dra (Billington & Marsh 1996) who suggested that non-kinematic broadening, such as Stark broadening, could be responsible.

3.4.4 Spiral shocks in quiescence

Figure 9 reveals the presence of weak spiral structure near the level of the continuum (we refer here to the structure within 1000 km s^{-1} of the centre of the images). In Figure 10 we show the maps with contours of spiral shocks observed during outburst (Steeeghs, Morales-Rueda & Groot in preparation) which line up well with the asymmetries that we see in quiescence. This spiral structure has been previously reported for U Gem in outburst (Groot 2001), making it one of a handful of systems in which the phenomenon has been detected. We emphasize that the amplitude of the spiral structure we find here is *far* less than that suggested by Neustroev and Borisov (1998) for the same system. Their data shows pronounced asymmetries, but were taken with poor spectral and phase resolution, and most importantly, without complete orbital coverage. In contrast our raw maps

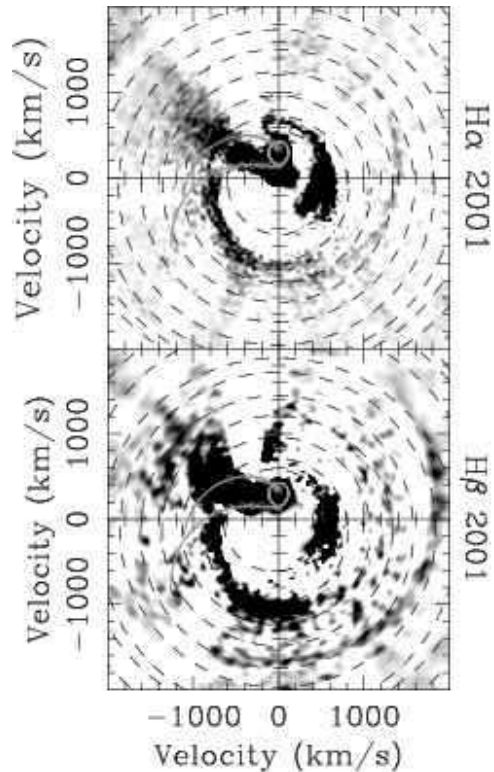


Figure 9. $H\alpha$ and $H\beta$ tomograms after subtraction of an elliptical background. The ellipses used to interpolate the background are plotted with dashed lines. The grey solid lines are the Keplerian disc and ballistic stream velocities for the stream path. The tomograms are saturated at only 3% of the maximum level of the unsubtracted maps.

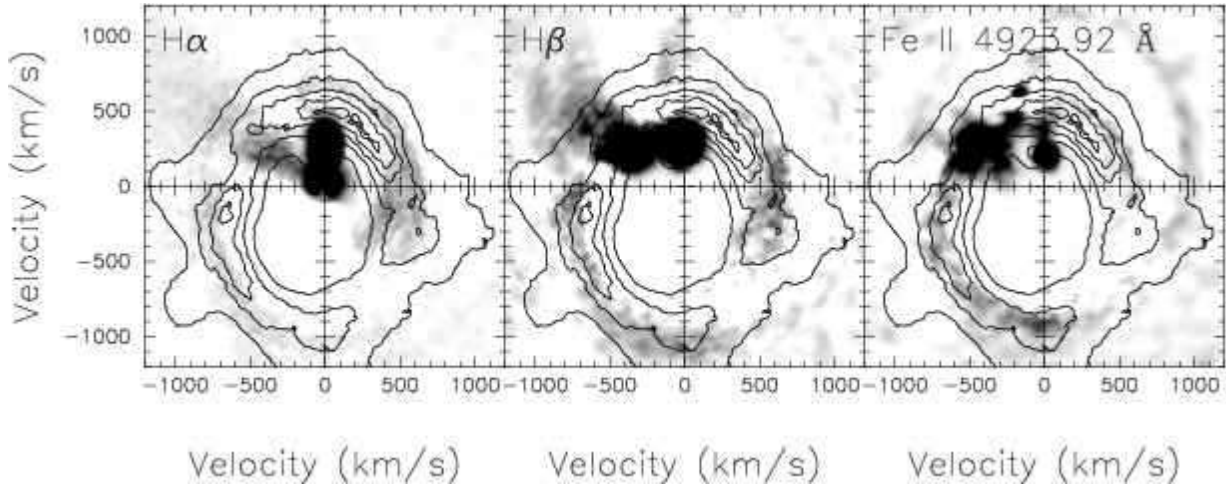
are very symmetric. We believe their claim of strong spiral structure to be incorrect, and a result of the difficulty of interpreting the complex variations of U Gem with inadequate orbital coverage.

The presence of spiral structure in the disc has been regarded as evidence of “spiral shocks” (Steeeghs, Harlaftis & Horne 1998), which had been predicted in simulations of accretion discs (see Matsuda et al. 2000 for a review). The spiral shock interpretation requires the presence of large or unusually hot discs. This prompted Smak (2001) and Ogilvie (2002) to propose alternatives to the spiral shocks to explain the phenomenon. They suggest that the spiral features revealed by Doppler tomography could be explained as the consequence of 3-body effects (Paczynski 1977). Ogilvie extends the model of Paczynski from 2 to 3 dimensions, allowing for a complete set of physical conditions in his model. He concludes that, due to tidal distortions, some regions of the disc would thicken, later being irradiated by the white dwarf. The pattern of thickening would be slightly spiral, but no waves or shocks would be involved in the process. In Doppler tomography the pattern would show up as the kind of open spiral structure seen in published tomograms.

These two competing explanations predict a different evolution of the spiral structures from outburst to quiescence. The spiral shock model requires hot material to have open spirals. In quiescence, the spirals, if present, are expected to be relatively tightly wound (Steeeghs and Stehle

Table 2. Summary of known Doppler tomographic reports of low velocity emission. Under 'State', Q means 'quiescence', O means 'outburst', and NA means 'not applicable'. WD stand for 'white dwarf' and S1996 for 'Steege et al. (1996)'.

System	State	Lines	Suggested source	Reference
IP Peg	O	H α	Irradiated slingshot prominences	S1996
SS Cyg	O	Balmer, He I, He II	Irradiated slingshot prominences	S1996
AM Her	NA	SI IV 1394Å, NV 1239Å	As in S1996	Gänsicke et al. (1998)
GP Com	NA	He I, He II	WD (Morales-Rueda et al. 2003)	Marsh (1999)
V426 Oph	Q	H α	As in S1996	North et al.(2001)
U Gem	Q	H α , He I	As in S1996	This paper

**Figure 10.** Doppler tomograms for the Balmer lines and Fe II after the symmetrical part around $(0, -107.1) \text{ km s}^{-1}$ is subtracted. The tomograms are saturated at 20 per cent of peak level. Superimposed on these tomograms we display isophotes (at 10, 30, 50, 70 and 90 per cent of peak level) from a tomogram based on outburst observations of U Gem (Steege, Morales-Rueda & Groot, in preparation).

1999). Assuming that the asymmetries that we see are indeed related to the outburst spiral structure, our observations show little change in morphology from outburst to quiescence, i.e. the spirals do not appear tightly wound. This argues against the spiral shock model as an explanation of the spiral structure detected in U Gem and favours Ogilvie's (2002) and Smak's (2001) explanation.

Although similar patterns are seen in several lines, we remain cautious about claiming a definitive detection of spiral structure in the quiescent U Gem. We emphasize again that the maps are really extremely symmetrical, and given the presence of strong bright-spot components which have strengths modulated in orbital phase, it is hard to rule out the possibility that we are seeing low-level artefacts. It is also worth noting that the size of the disc we find from the bright-spot of $\sim 0.3a$ (Section 3.4.1) is close to the minimum observed radius of U Gem's disc (Smak 1984) and well inside the tidal radius where one would expect Ogilvie's and Smak's model to operate, let alone tidally-driven spiral shocks.

3.4.5 Disc shielding

A notable feature in most of the tomograms, in particular in Fe II, is the mass donor's irradiated face. Small sections of these maps, centered on the donor star, are presented in the top row of Figure 11. The figure shows that the irradiation-induced emission avoids the equator of the mass donor, in-

dicative of shielding by the disc (Harlaftis 1999; Morales-Rueda et al. 2000). The irradiation in H α and H β seems to be located further from the L1 point than for the other lines. This is suggestive of a changing effective thickness due to wavelength dependent opacity at the EUV wavelengths needed for photoionisation of the elements involved. This has been previously seen in other CVs (Morales-Rueda et al. 2000).

In the bottom row of Figure 11 we show simulated tomograms for a system with the same parameters of U Gem but with varying height-to-radius ratio (H/R) in the disc. We included some broadening in the simulations by convolving the synthetic datasets with a gaussian with FWHM 15 km s^{-1} . Values of H/R from 0.10 to 0.25 were considered (increasing by 0.05 each time). For $H/R > 0.30$, the height completely prevents the irradiation to take place. We estimate from this that the H/R ratio for U Gem is ~ 0.15 (He I), ~ 0.20 (Fe II) and ~ 0.25 (H α and H β). These values could be a little smaller if K_2 is larger than we have assumed (raising the Roche lobes of Figure 11), as suggested by the sharp spot in He II (section 3.4.1).

3.5 Inclination angle

Zhang & Robinson (1987) derived an orbital inclination angle $i = 69.7^\circ$ for U Gem from a detailed lightcurve fitting model. Other estimates of i have displayed a trend to somewhat smaller values, but mainly in the region of $65^\circ < i <$

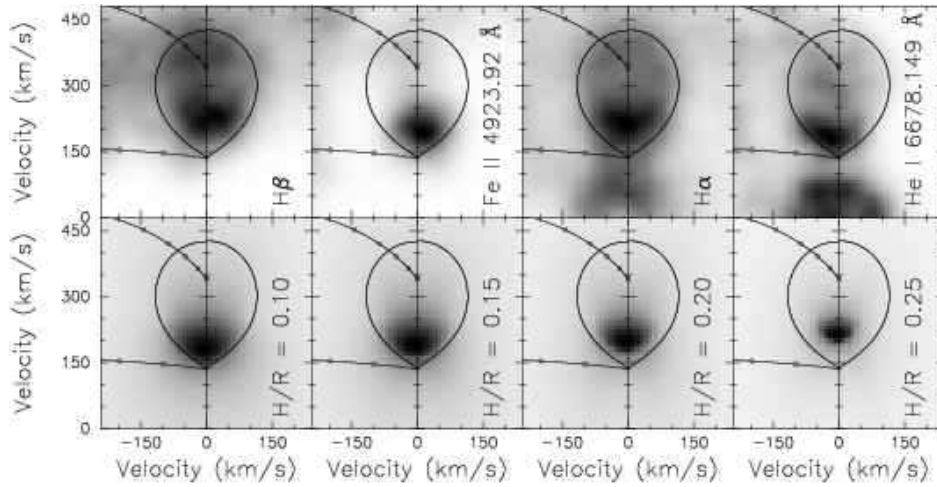


Figure 11. Real and simulated disc shielding. The top row is a close view of those tomograms centered on the mass donor. The lower portion of the Roche lobe is not fully irradiated, which is explained by shielding of the mass donor’s equatorial regions due to an effective height of the disc’s outer rim. The bottom row shows simulations for different H/R ratios. All the images are saturated at 100 per cent, the colour scales starting at zero flux.

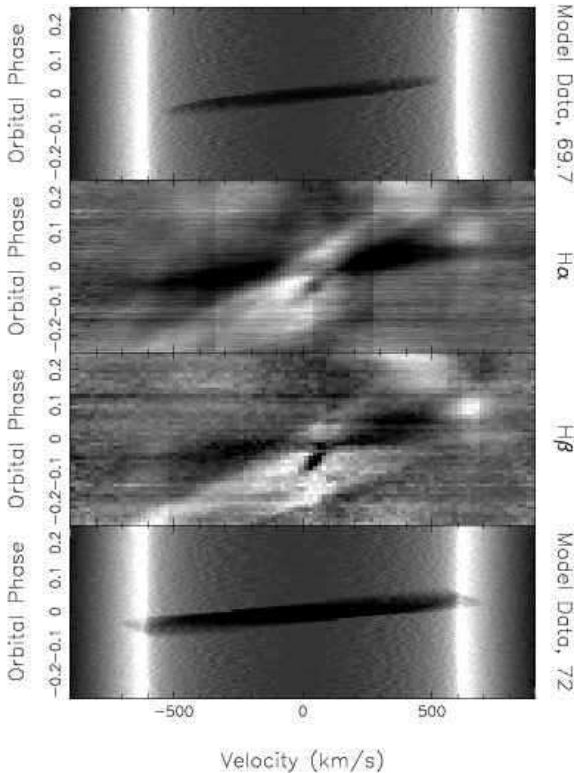


Figure 12. The top and bottom panel show simulated data of the eclipse of the emission lines for 69.7° and 72° respectively. The central panels show data from the Balmer lines. The central panels were processed to improve visibility of the extension of the eclipse (see text for details). All the panels are saturated at 100 per cent. Note that the data are affected by emission components not included in our simulations.

70° . Given the radial velocity semi-amplitudes, the inclination determines the component masses. Long (2000) and more recently Naylor et al (2005) encountered a problem when combining a measurement of the gravitational redshift

of the white dwarf, which fixes M/R , with other constraints including inclination estimates. The problem, summarised in Fig. 8 of Naylor et al. is that the gravitational redshift gives a rather small radius for a given mass, which only crosses the Hamada-Salpeter mass-radius relationship for M_1 $1.25 M_\odot$ implying at the same time a low inclination of $i \sim 65^\circ$ and a radius well below the value predicted from U Gem’s UV spectrum and parallax (Long 2000; Harrison 1999). The Hamada-Salpeter relation and the radius measured from the UV flux are in agreement for a much higher inclination of 72° to 74° and a lower white dwarf mass, $\sim 1.05 M_\odot$ (Naylor et al. 2005), but then one must suppose that the gravitational redshift, a combination of careful measurements from the UV (Long & Gilliland 1999) and I-band (Naylor et al. 2005) to be seriously in error.

In this section we use the eclipse of the emission lines, and specifically the highest velocity in the lines that is eclipsed to provide a new independent constraint on the orbital inclination. We find a high inclination favouring the low-mass solution for the white dwarf. The key point is that in a partially eclipsing system, since the eclipse does not reach the white dwarf, there will be a velocity in the lines above which there is no eclipse. If we can determine this point, we can measure the inclination. We do so by simulating the eclipse and comparing the simulation with the data (Figure 12). The top panel shows a simulated trailed spectra when i is set to 69.7° , with K_1 and K_2 set to the values mentioned before. The three central panels show real data after removal of the mean spectrum. The extension of the eclipse in these panels easily reaches 700 km s^{-1} while in the simulated data of the top panel it does not go beyond 550 km s^{-1} . The inclination must be larger than 69.7° ; we favour a value of $i \sim 72^\circ$ (lowest panel, Figure 12).

The emission line eclipse strongly favours the low-mass, high inclination solution and is in conflict with the measurements of gravitational redshift. Our data allows us to check the systemic-velocity of the donor star which is one component of the gravitational redshift. We did this by subtracting from the dataset the orbital motion corresponding to the

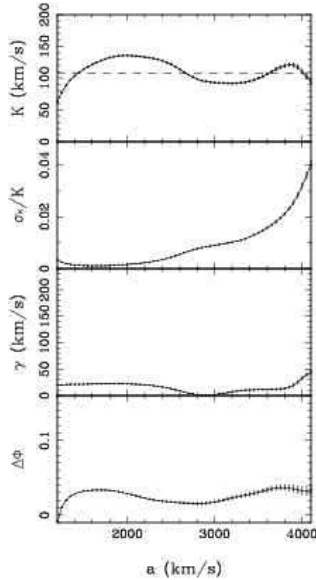


Figure 13. The diagnostic diagram for H α . A separation of Gaussians equal to $\sim 3400 \text{ km s}^{-1}$ seems appropriate to avoid most of the jump in noise close to 4000 km s^{-1} in the σ_K/K plot. This separation corresponds to a plateau in the K plot, from which the value $\sim 95 \text{ km s}^{-1}$ is read for K_1 . The dashed horizontal line in the top panel marks the level 107.1 km s^{-1} .

centroid of the mass donor’s irradiated region. Then we averaged the spectra in phase ranges for which the separation between the signal from the irradiated region and other contaminating signals (bright spot, disc) was maximum. This produced well defined peaks to which we fitted Gaussian solutions. We calculated the systemic-velocity of the donor as the offset of the centre of the Gaussians with respect to their wavelengths at rest. The result is $36 \pm 2 \text{ km s}^{-1}$ (average of H α , H β and Fe II). This is compatible with $29 \pm 6 \text{ km s}^{-1}$ from Naylor et al. (2005) but, being higher, it reduces a little the value of the redshift. However, this reduction is far from enough to resolve the discrepancy between the two mass solutions for U Gem.

3.6 Orbital velocity of the white dwarf

The value of K_1 for U Gem is known accurately thanks to a direct observation of metal lines from the white dwarf’s surface (Long & Gilliland, 1999). The result, $107.1 \pm 2.1 \text{ km s}^{-1}$, can be used to test the effectiveness of the techniques already in use, which are mostly based on assuming that the emission lines originated on the accretion disc will provide information from which the motion of the white dwarf can be tracked.

Two traditional techniques to measure K_1 are the diagnostic diagram (Shafter, Szkody & Thorstensen 1986) and the light-centre diagram (Marsh 1988). Both use the double-Gaussian method (Schneider & Young 1980; hereafter SY80) to measure the radial velocities from a dataset. This method consists in convolving the continuum subtracted line with two Gaussians of identical width and varying separations.

In the diagnostic diagram technique, the velocities measured are then fitted with an orbital solution $V = \gamma - K \sin(2\pi[\phi - \Delta\phi])$, and the parameters of the fit are plotted

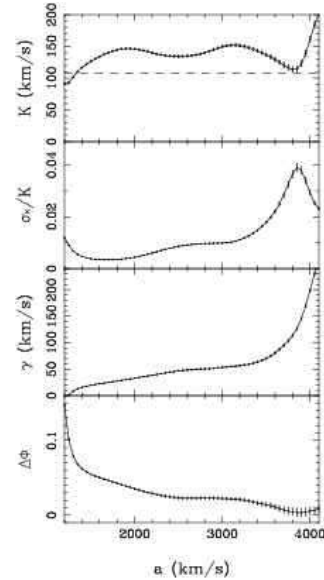


Figure 14. The diagnostic diagram for H β . A separation of 3000 or 3200 km s^{-1} seems appropriate in this case. This points to a value of 150 km s^{-1} for K_1 . The dashed horizontal line in the top panel marks the level 107.1 km s^{-1} .

in a diagram like those presented in Figs. 13 and 14. K_1 is considered to coincide with K when K is stable over a range of Gaussian separations (a in the plot) or at the point just before σ_K/K increases sharply. In Figs. 13 and 14 we see that this happens for $a = 3400 \text{ km s}^{-1}$ giving values of $K_1 = 95$ and 150 km s^{-1} for H α and H β respectively. The plots in the diagnostic diagrams display curves that behave only partially as expected. In particular there is no simultaneous convergence towards final values in the panels (compare, for instance, top and bottom panel of Figure 13).

In the light-centre technique, the radial velocities measured using the double-Gaussian method are plotted in velocity space and the line of points obtained is extrapolated towards the K_y axis. The value for K_1 is the point at which the extrapolated line crosses K_y . The plot obtained, not reproduced here, is very similar to Figure 15, which is described below.

3.6.1 A new method to measure K_1

A problem with the double Gaussian measurement is that each spectrum is treated one by one, before the individual radial velocities are fitted by a sinusoid. The process breaks down as soon as the signal-to-noise in one of the spectra becomes too low for the measurements to be made. We can do somewhat better by fitting all spectra simultaneously, still employing the double-gaussian method because of its isolation of particular velocities in the line profiles. Denoting the velocity, flux and uncertainty of the i -th pixel of the j -th spectrum by v_{ji} , f_{ji} and σ_{ji} respectively, we therefore minimise the following function:

$$\sum_{j=1}^N w(\mathcal{V}_{ji}) \left[\sum_{i=1}^M f_{ji} g(\mathcal{V}_{ji}) \right]^2 \quad (1)$$

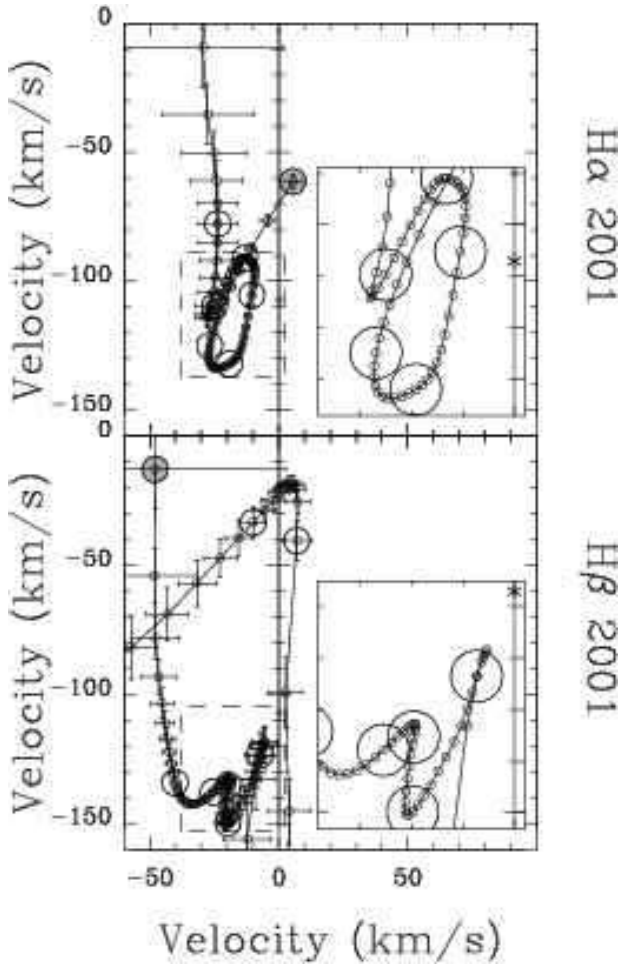


Figure 15. The result of applying our new method to H α and H β . See text for details of how to read the plots. A certain trend of the points in direction to (0,107.1) km s⁻¹ is seen twice in the H β plot. H α shows no clear trend towards (0,107.1) km s⁻¹.

where \mathcal{V}_{ji} is the velocity of a pixel relative to the velocity of the spectrum U_j ,

$$\mathcal{V}_{ji} = v_{ji} - U_j, \quad (2)$$

w is a weighting function given by

$$w(\mathcal{V}_{ji}) = \frac{1}{\sum_{j=1}^M \sigma_{ji}^2 g^2(\mathcal{V}_{ji})}, \quad (3)$$

and g represents two gaussians of standard deviation σ_G separated by a_G ,

$$g(v) = \exp\left(-\frac{(v - \frac{1}{2}a_G)^2}{2\sigma_G^2}\right) - \exp\left(-\frac{(v + \frac{1}{2}a_G)^2}{2\sigma_G^2}\right) \quad (4)$$

The function of Eq. 1 is minimised by fitting the velocities of the spectra U_j , $j = 1$ to N . If these quantities were fitted independently, then we are back to the standard double gaussian method for one spectrum which finds the velocity U for which $\sum_i f_i g(v_i - U) = 0$. The difference is that we do not allow the U_j to be independent, but instead constrain them to represent a circular orbit as so:

$$U_j = \gamma - K_x \cos(2\pi\phi_j) + K_y \sin(2\pi\phi_j), \quad (5)$$

fitting instead the standard orbital parameters γ , K_x and K_y . Uncertainties were estimated by a bootstrap procedure (Diaconis & Efron 1983), with 1000 bootstrap samples being chosen from the original set of spectra.

The end products are K_x and K_y values as a function of gaussian separation, exactly as with the old procedure. The gain is greater robustness in the presence of noise.

Figure 15 shows the application of this new method for performing the analysis of radial velocities. We use a small cross to mark the point with coordinates (0,-107.1) km s⁻¹, the direct measurement for K_1 from Long & Gilliland (1999). The points in the diagrams show the variation with separation for two gaussians of FWHM = 100 km s⁻¹. The initial separation is 1200 km s⁻¹ and is marked with a large grey circle. Small circles mark steps of 50 km s⁻¹ while large circles marks steps of 500 km s⁻¹. In both panels an inset with a blow up of the region close to (0,-107.1) km s⁻¹ has been included. In the insets we have omitted the error bars.

Although the H β plot does on two occasions shows trends towards the known value, it would be impossible in the absence of Long & Gilliland's value to deduce it from our measurements, although they are at least in its vicinity. This should not come as a surprise; the diagnostic diagrams have a phase offset from zero, and whatever causes the distortion will distort the new method as well. The chief conclusion is that even far in the wings, there is something that distorts the radial amplitudes by of the order 20 to 50 km s⁻¹, and that we cannot improve on Stover's (1981) estimate of 137 ± 8 km s⁻¹.

We carried out several simulations to see what could disturb the wing velocities using the model applied in Section 3.5. We began the simulations considering just an accretion disc and an opaque secondary star. In this way we obtained double-peaked phase-shifted spectra in which an eclipse by the secondary star was included but no flux was contributed by it to the spectra. We found that both techniques were able to accurately recover the correct value for K_1 from this dataset. We then added a nearby line so that the separation and relative fluxes of both lines would approximate the situation of having He I or Fe II close to H α or H β respectively. Again both methods correctly extracted K_1 from the data. Then we added a bright spot (its parameters tuned to fit the feature observed in our data) to the main line (H α -like and H β -like) and found that the measurements were seriously distorted by its presence. However, after increasing the gaussian separation beyond ~ 2000 km s⁻¹ the methods again reliably extracted K_1 from the data. Lastly, we added a bright spot to the companion lines (He I -like and Fe II-like) and found that the recovery of K_1 was no longer possible.

In summary, we cannot recover U Gem's K_1 to better than ~ 40 km s⁻¹, and we suspect that the problem is caused by the need to go far into the line wings to avoid the bright-spot, which brings with it the problem of contamination by the bright-spot emission of nearby lines.

4 CONCLUSIONS

We have presented high spectral resolution and signal-to-noise optical spectra of U Gem with the aim of testing the use of the broad emission lines in tracing the motion of the

accreting white dwarf in CVs. U Gem is particularly well suited for this task because the true motion of its white dwarf has been measured from *HST* spectra by Long et al (1999).

Despite observations on a 4m-class telescope of one the brightest dwarf novae, we find values of the semi-amplitude of the white dwarf ranging from 80 to $\sim 150 \text{ km s}^{-1}$ which contain not a hint that the correct value is the 107 km s^{-1} measured by Long et al (1999). Neither the diagnostic diagram (Shafter et al 1986) nor the light centre technique (Marsh 1988) were of any help. The root cause of the problem seems to be the bright-spot which causes an asymmetry that extends to large velocities in Doppler maps, and which is present in the same way in pairs of close spectral lines (H α and He I ; H β and Fe II), thus violating the usual assumption of a trend towards symmetry at high velocity.

Our data reveal a number of new phenomena for which we can offer only tentative explanations. These include low velocity absorption and emission that we suggest imply the presence of prominences on the mass donor star.

U Gem shows a complex structure in the region of the gas stream/impact region. Extended emission lies between the velocity expected for the ballistic gas stream directly and the velocity of the Keplerian disc along the gas stream. This emission extends both to very high and very low velocities in the maps. Most surprising of all is the presence of a narrow component of the bright-spot in He II, which appears to be unresolved even at $R \approx 10,000$. This narrow spot appears to come from the disc rather than the stream, but seems to require a slightly larger value of radial velocity amplitude for the secondary star than has been measured to date.

We find no evidence of stream overflow, but we find weak spiral asymmetry in the (quiescent) disc, similar in nature to those seen during outburst. This may provide support for Ogilvie's and Smak's explanation for the presence of spiral structure based upon 3-body effects.

We find an inclination angle of $\sim 72^\circ$. This supports a solution for the mass of U Gem's white dwarf in agreement with the Hamada-Salpeter mass-radius relationship and with the radius measured from the UV flux. This reinforces the discrepancy first noted by Naylor et al. (2005) regarding the mass estimated from gravitational redshift. This constitutes an important open puzzle.

ACKNOWLEDGMENTS

EU was supported by PPARC (UK) and Fundación Andes (Chile) under the program Gemini PPARC-Andes throughout most of this research. LMR was supported under a PPARC PDRA grant and TRM under a PPARC SRF during some of the period over which this work was undertaken.

Danny Steeghs' comments about sections of this article greatly improved the final version. We also wish to thank him for his Doppler map of U Gem in outburst.

The authors acknowledge the data analysis facilities provided by the Starlink Project which is run by the University of Southampton on behalf of PPARC.

This research has made use of NASA's Astrophysics Data System Bibliographic Services, as well as of the wonderful resources provided by Hartley Library at the University of Southampton.

During the long time that took the writing of this article, Soledad Martínez Labrín had to use many times her incredible ability to make starry the darkest nights. EU is lovingly indebted to her.

REFERENCES

- Armitage, P., Livio, M., 1998, *ApJ*, 493, 898
 Bessell, M., 1999, *PASP*, 111, 1426
 Burke, P., 1987, *Byte Magazine* (July)
 Cabrera, J., Meer, P., 1996, *IEEE Trans. PAMI*, 18, 752
 Collier Cameron, A. et al., 1999, *MNRAS*, 308, 493
 Diaconis, P., Efron, B., 1983, *Sci. Am.*, v. 248, n. 5, 96
 Eggleton, P., 1983, *ApJ*, 268, 368
 Fitzgibbon, A., Pilu, M., Fischer, R., 1999, *IEEE Trans. PAMI*, 21, 476
 Friend, M., Martin, J., Smith, R., Jones, D., 1990, *MNRAS*, 246, 637
 Greenstein, J., Kraft, R., 1959, *ApJ*, 130, 99
 Groot, P., 2001, *ApJ*, 551, L89
 Harlaftis, E., 1999, *A&A*, 346, L73
 Harrison, T. et al., 1999, *ApJ*, 515, 93
 Jędrzejewski, R., 1987, *MNRAS*, 226, 747
 Kent, S., 1983, *MNRAS*, 266, 562
 Kunze, S., Speith, R., Hessman, F., 2001, *MNRAS*, 322, 499
 Livio, M., Soker, N., Dgani, R., 1986, *ApJ*, 305, 267
 Long, K., Gilliland, R., 1999, *ApJ*, 511, 916
 Lubow, S., 1989, *ApJ*, 340, 1064
 Marsh, T., 1988, *MNRAS*, 231, 1117
 Marsh, T., 1989, *PASP*, 101, 1032
 Marsh, T., Horne, K., 1988, *MNRAS*, 235, 269
 Marsh, T., Horne, K., Schlegel, E., Honeycutt, R., Kaitchuck, R., 1990, *ApJ*, 364, 637
 Matsuda, T., Makita, M., Fujiwara, H., Nagae, T., Haraguchi, K., Hayashi, E., Boffin, H., 2000, *Ap&SS*, 274, 259
 Morales-Rueda, L. et al., 2000, *MNRAS*, 313, 454
 Naylor, T., Allan, A., Long, K., 2005, *MNRAS*, 361, 1091
 Neustroev, V.V., Borisov, N.V., 1998, *A&A*, 336, L73
 Ogilvie, G., 2002, *MNRAS*, 330, 937
 Osaki, Y., 1996, *PASP*, 108, 39
 Paczynski, B., 1977, *ApJ*, 216, 822
 Schneider, D., Young, P., 1980, *ApJ*, 238, 946
 Shafter, A., Szkody, P., Thorstensen, J., 1986, *MNRAS*, 308, 765
 Shanno, D., Phua, K., 1980, *ACM Tran. on Mathematical Software*, 6, 618
 Smak, J., 2001, *Acta Astron.*, 51, 279
 Smak, J., 2001, *Acta Astron.*, 51, 295
 Smith, M. et al., 1998, *ApJ*, 507, 94
 Smith, M., Dhillon, V., Marsh, T., 1998, *MNRAS*, 296, 465
 Steeghs, D., Harlaftis, E., Horne, K., 1998, *MNRAS*, 296, 463
 Steeghs, D., Horne, K., Marsh, T., Donati, J., 1996, *MNRAS*, 281, 626
 Steeghs, D., Stehle, R., 1999, *MNRAS*, 307, 99
 Stover, R., 1981, *ApJ*, 249, 673
 Wade, R. et al., 1981, *ApJ*, 246, 215
 Watson, C., Dhillon, V., Rutten, R., Shocope, A., 2003, *MNRAS*, 341, 129
 Welsh, R., Horne, K., Gomer, R., 1995, *MNRAS*, 275, 649
 Zhang, E., Robinson, E., 1987, *ApJ*, 321, 813

APPENDIX A: ELLIPSE FITTING OF DOPPLER MAP ISOPHOTES

In a Doppler tomogram is usually possible to find at least two closed contours at a particular flux level. This happens

because the tomogram is usually dominated by the disc continuum, in such a way that the flux increases from the centre of the map towards a ring of maximum intensity, the flux then decreasing from this ring outwards. This scenario makes the traditional methods to fit ellipses from the field of galactic surface photometry unstable (e.g. Kent 1983, Jędrzejewski 1987), because in them most levels occur only once. On the other hand, the techniques employed in computer vision, for the characterization of conics in an image, are very suitable for application here. We devised a new strategy by dividing the problem in two stages:

- (i) Selection of points pertaining to a closed contour, at a given level of flux.
- (ii) Fitting of an ellipse to such points.

A1 First stage

Tracing the contours at a certain level and extracting the points pertaining to a single closed contour at the same level are two completely different problems. The former is readily solved in a purely graphical manner (e.g. Burke 1987), while the latter (ours) is non-trivial and, as far as we know, not certainly solvable without human assistance. Consequently the first stage admits several approaches varying in efficiency. We devised one in which from many angular directions either zero or one pixel was chosen, according to its proximity to the pixel selected in the previous direction and to the general pattern of the contours (e.g. no crossed contours were allowed).

The procedure could be carried out almost on its own in the case of a smooth continuum, but it required close supervision when dealing with finely detailed (or noisy) structure. The main danger is for the algorithm not to close the contour or to take a wrong detour before coming back to the expected path.

A2 Second stage

Once all the points for a particular level were chosen, we fitted them with ellipses according to an analytical ellipse-specific method proposed by Fitzgibbon, Pilu & Fischer (1999). The task is accomplished via a very efficient matrix procedure. In a non-matrix form we can explain the procedure as the fitting of a general conic of the form:

$$Ax^2 + Bxy + Cy^2 + Dx + Ey + F = 0 \quad (\text{A1})$$

but adding the constraint:

$$4AC - B^2 = 1 \quad (\text{A2})$$

so that the result will specifically be an ellipse. The constraint adds an arbitrary factor of scaling to the solution, but the algorithm provides for the removal of the effect at a later stage. The resulting general coefficients A , B , C , D , E and F were converted to the more meaningful values V_{xc} , V_{yc} (coordinates of the centre of the ellipse), a , b (size of the two semiaxes), e (eccentricity) and θ (angle of rotation). Uncertainties were estimated by a bootstrap procedure over the points.

The solution given by the method of Fitzgibbon et al. (1999) has been proved to be unique, but it must be noted that it has a certain bias to low eccentricities, specially if

only a few points are fed to the algorithm. This is fine for our purposes because we use many points for the fitting (basically limited by the resolution of the map) and also we do not want unrealistically high values for e (which for an accretion disc we expect to be close to 0 for most isophotes). If this was a problem, the bias could be removed by another bootstrap procedure at the cost of computing time (see, for instance, Cabrera & Meer 1996).

A3 Application: subtraction of elliptical background

By subtracting the disk from the original Doppler map we can greatly improve the visibility of asymmetrical features. Although we expect disc isophotes to have low values of e , this value is generally not be exactly 0. We therefore used the results from the ellipse-fitting process described above to subtract an interpolated elliptical background. To do this, we found for every point the two closest ellipses and then we linearly interpolated their fluxes according to the distance of the point to both ellipses. Special cases were: a point exactly in the path of an ellipse (its flux was used), and points beyond the region fitted (no flux was assigned).

In Figure (A1) we show an example of the performance of the method by using a synthetic Doppler map.

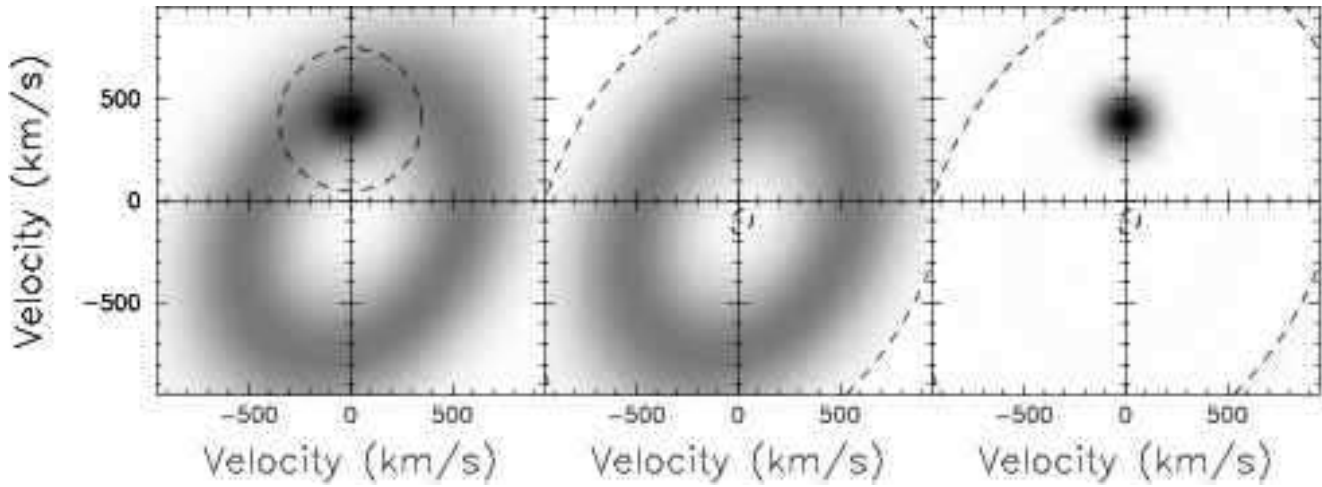
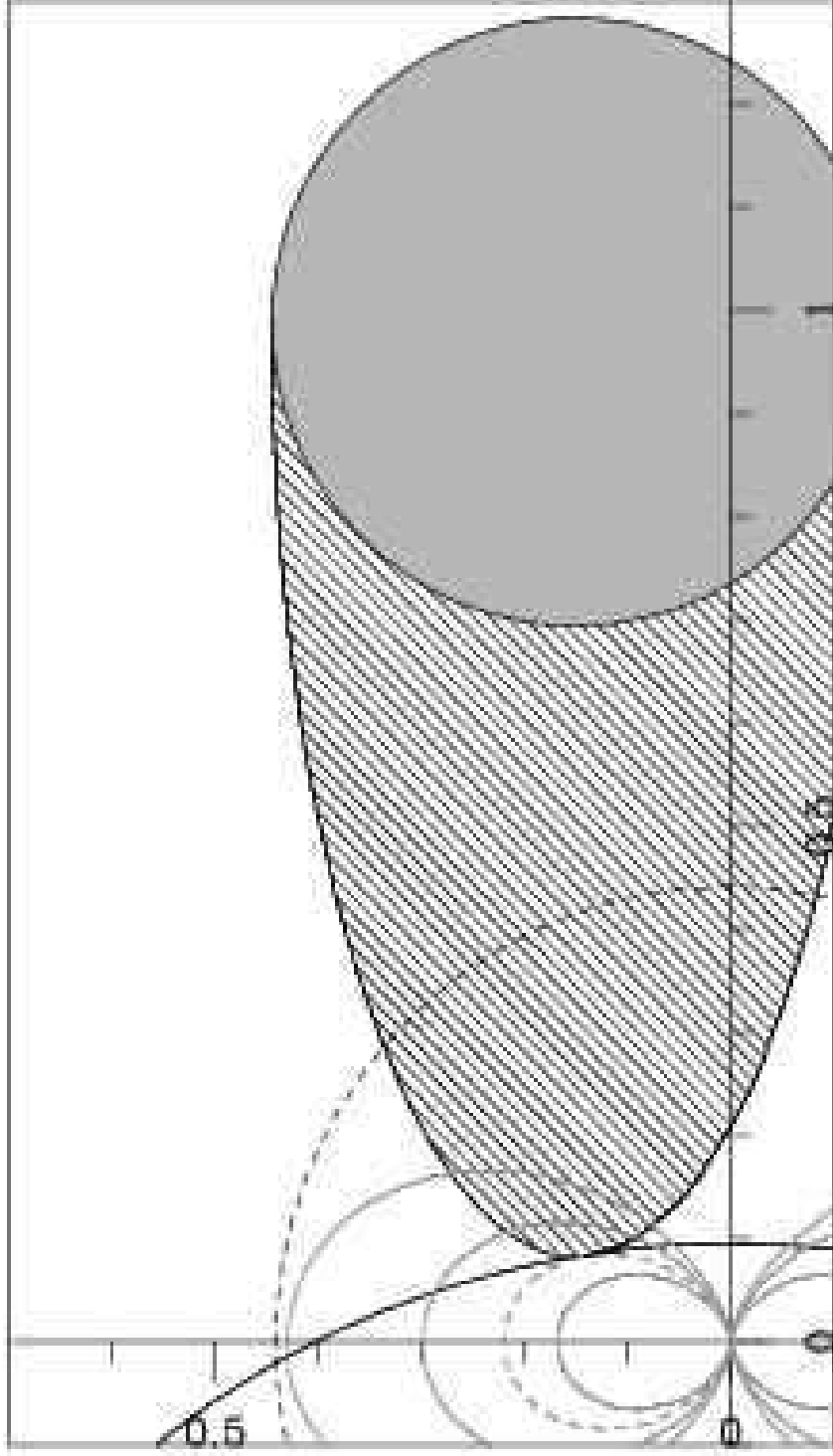
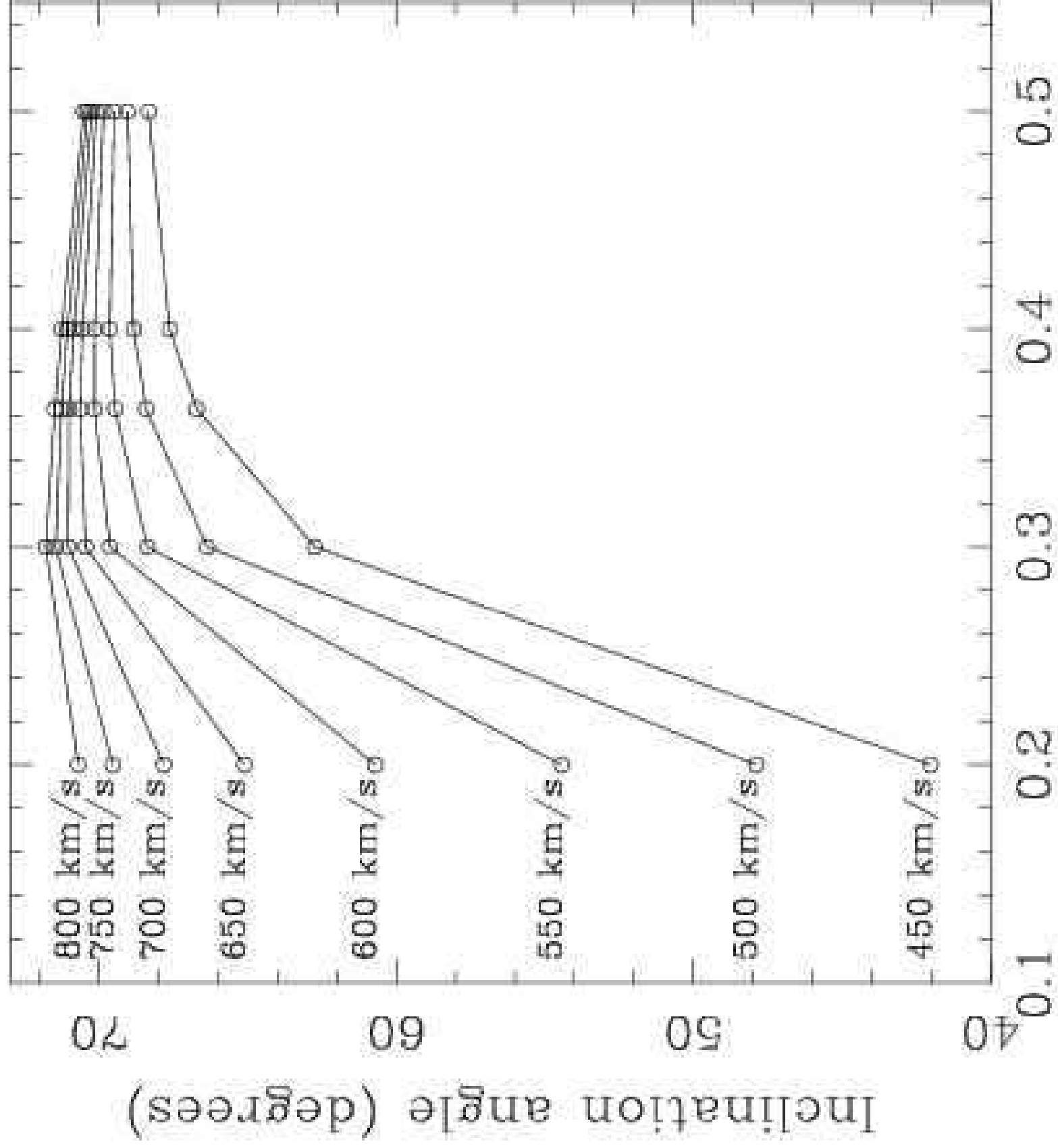


Figure A1. Performance of the elliptical background subtraction. The left panel shows a synthetic tomogram with an elliptical background and a spot of enhanced emission. The region inside the dashed circle was masked during the fitting of ellipses. The middle panel shows the continuum interpolated from the fitted ellipses. In both the middle and right panel the dashed ellipses are the innermost and outermost fitted ones. The right panel shows the result of subtracting the middle panel from the left one. The (correct) 2-dimensional Gaussian nature of the synthetic spot is made more evident in the right panel than it was in the original figure, in which it seemed to be elongated along the curvature of the disc.



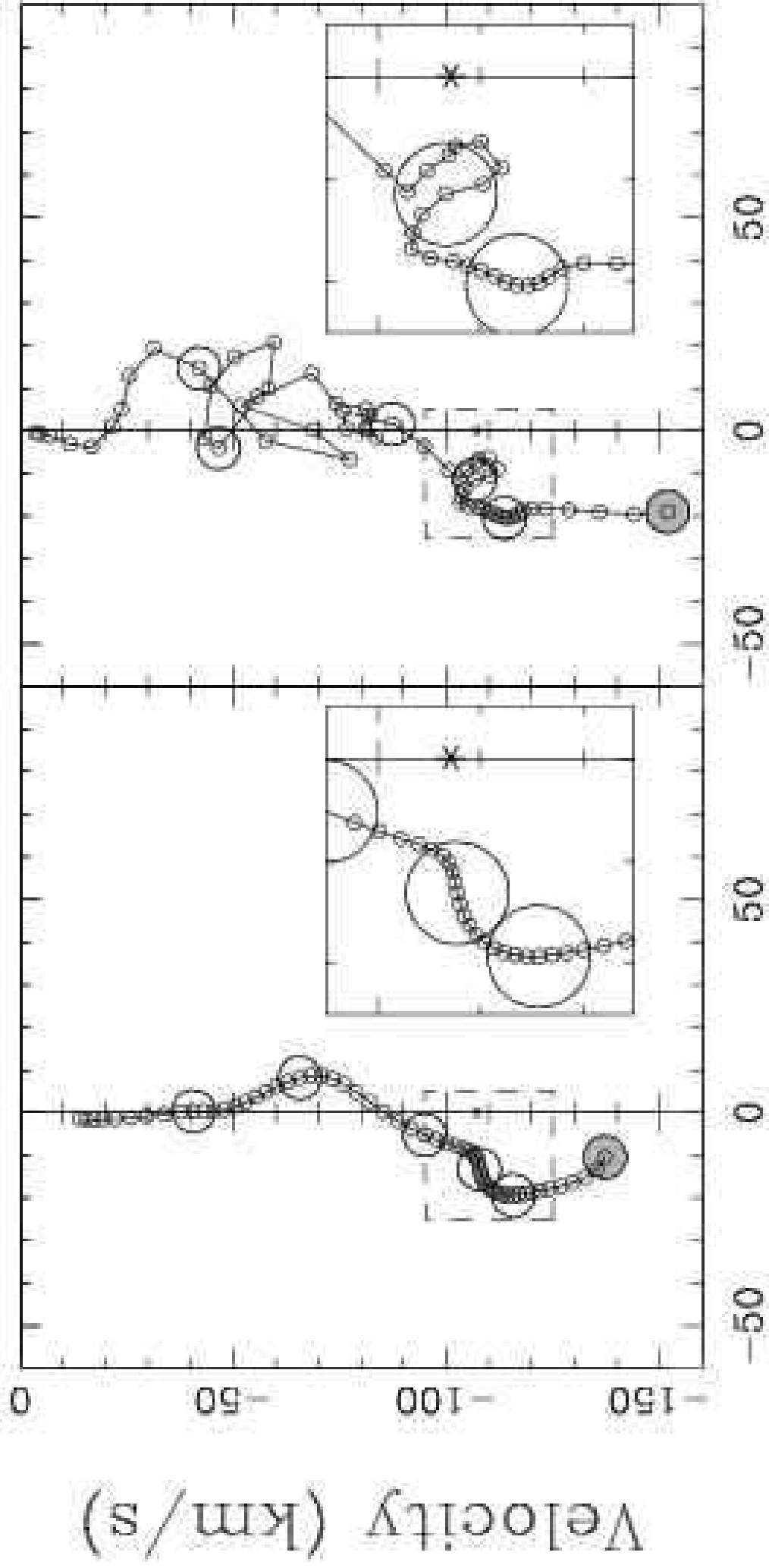
x (units of a)

y (units of a)

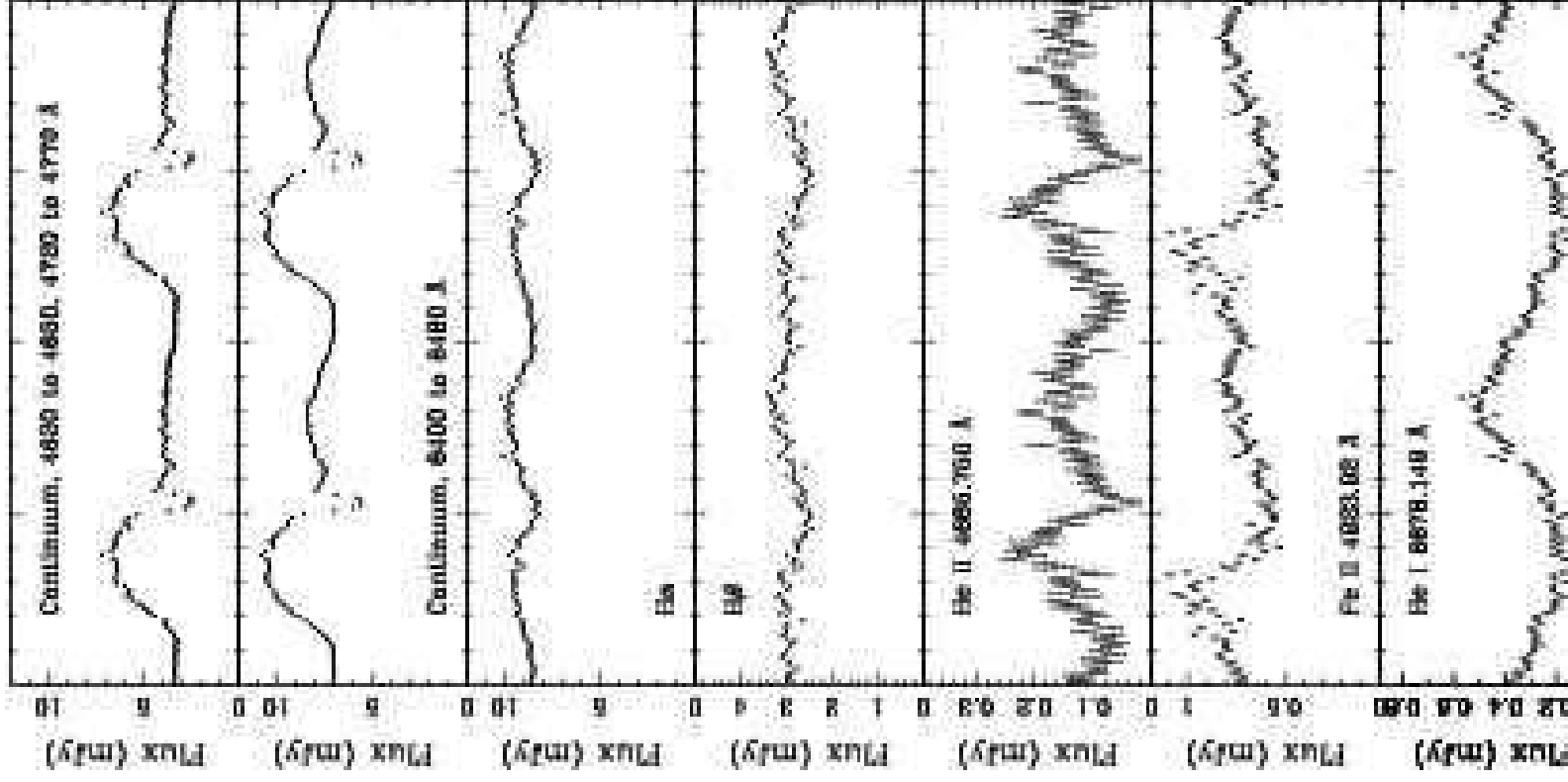


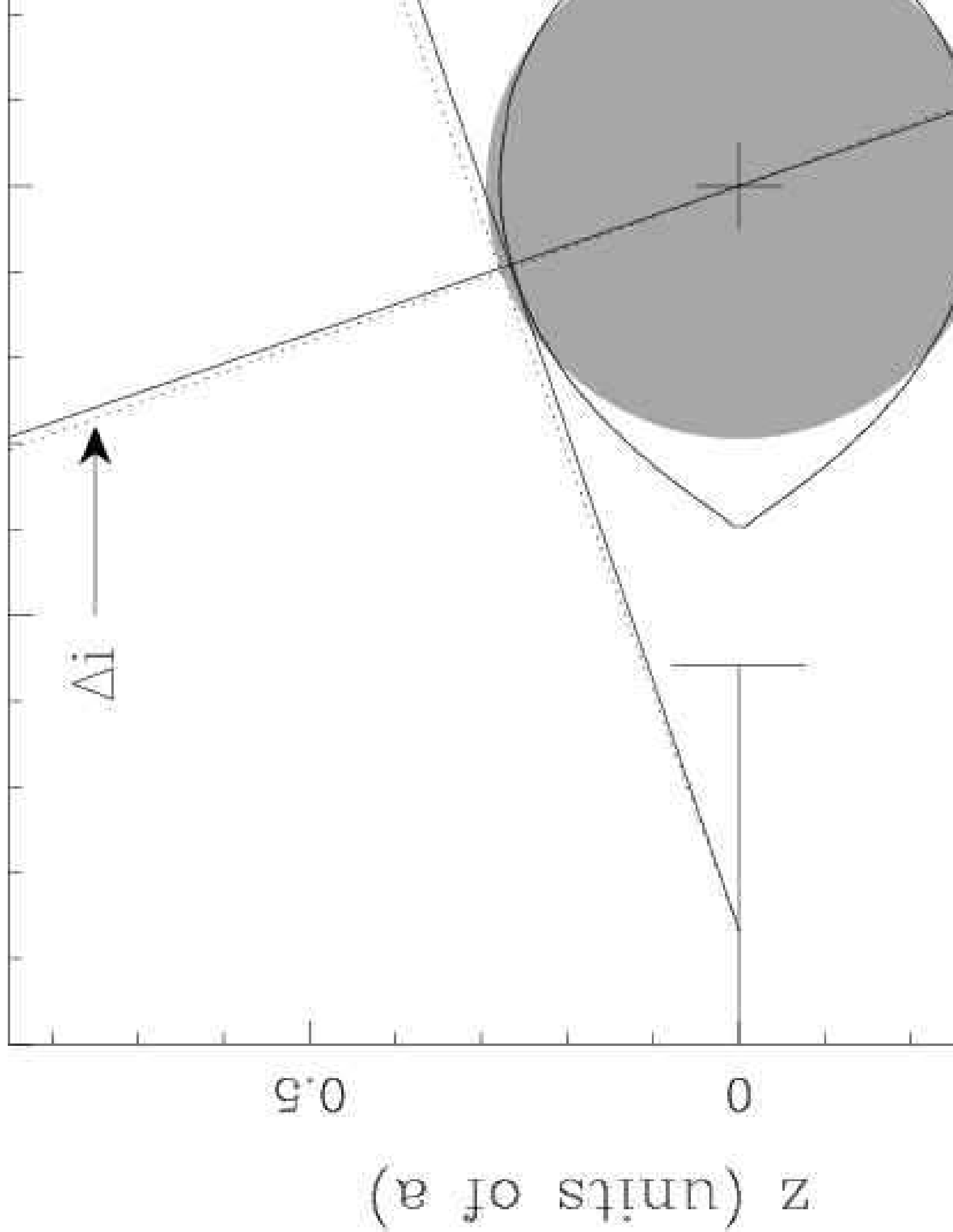
This paper

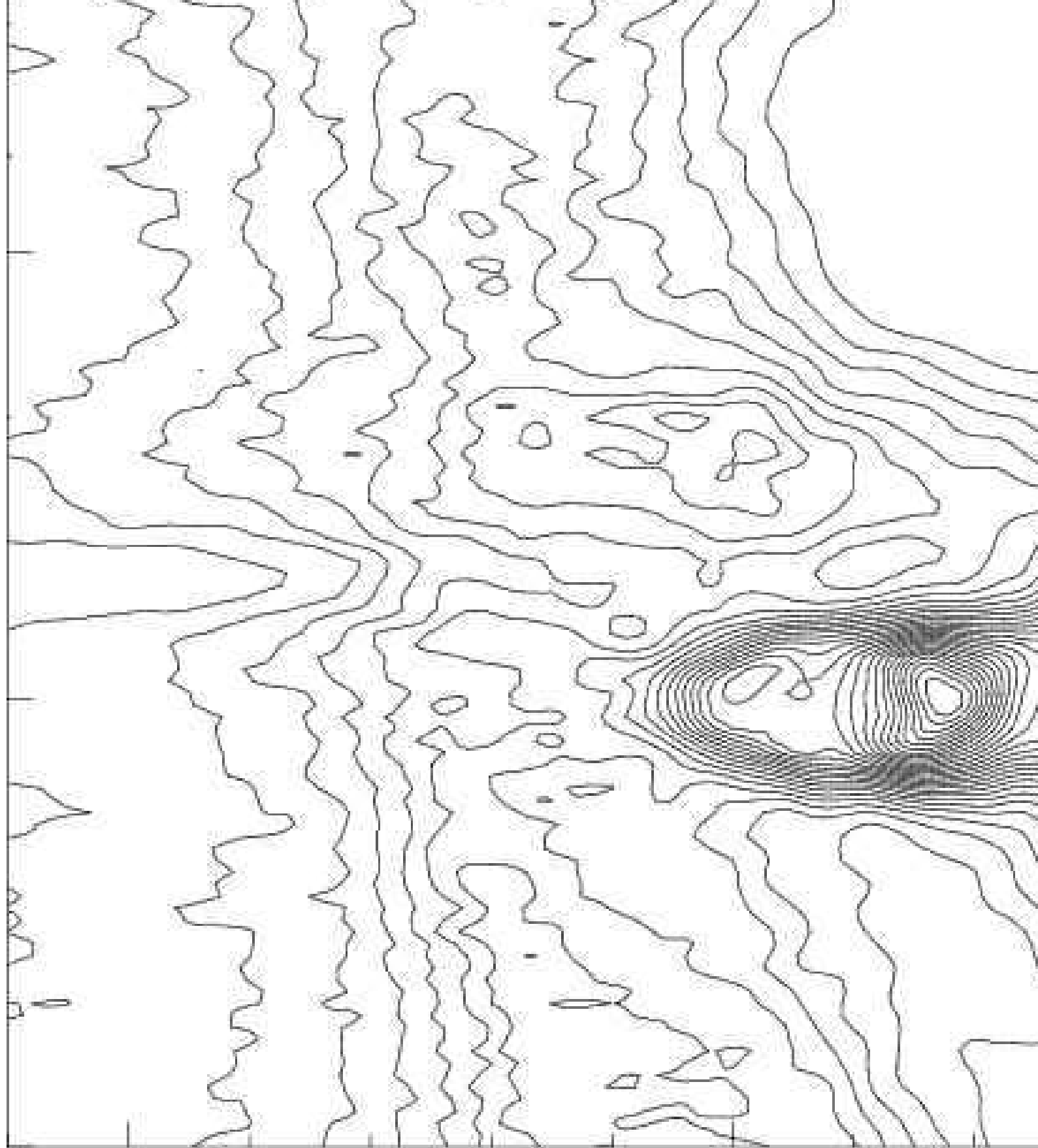
SY1980



Velocity (km/s) Velocity (km/s)







Radius (km/s)

500

1000

